


## Article

# Ex Vivo Determination of Broadband Absorption and Effective Scattering Coefficients of Porcine Tissue

Florian Bergmann <sup>\*</sup> , Florian Foschum, Leonie Marzel and Alwin Kienle

Quantitative Imaging and Sensors, Institut für Lasertechnologien in der Medizin und Meßtechnik an der Universität Ulm, Helmholtzstr. 12, D-89081 Ulm, Germany; florian.foschum@ilm-ulm.de (F.F.); leonie.marzel@stud.uni-heidelberg.de (L.M.); alwin.kienle@ilm-ulm.de (A.K.)

\* Correspondence: florian.bergmann@ilm-ulm.de

**Abstract:** A novel approach for precise determination of the optical scattering and absorption properties of porcine tissue using an optimized integrating sphere setup was applied. Measurements on several sample types (skin, muscle, adipose tissue, bone, cartilage, brain) in the spectral range between 400 nm and 1400 nm were performed. Due to the heterogeneity of biological samples, measurements on different individual animals as well as on different sections for each sample type were carried out. For all samples, we used an index matching method to reduce surface roughness effects and to prevent dehydration. The derived absorption spectra were used to estimate the concentration of important tissue chromophores such as water, oxy- and deoxyhemoglobin, collagen and fat.

**Keywords:** optical properties; biological tissue; integrating sphere



**Citation:** Bergmann, F.; Foschum, F.; Marzel, L.; Kienle, A. Ex Vivo Determination of Broadband Absorption and Effective Scattering Coefficients of Porcine Tissue. *Photonics* **2021**, *8*, 365. <https://doi.org/10.3390/photonics8090365>

Received: 5 August 2021

Accepted: 26 August 2021

Published: 31 August 2021

**Publisher's Note:** MDPI stays neutral with regard to jurisdictional claims in published maps and institutional affiliations.



**Copyright:** © 2021 by the authors. Licensee MDPI, Basel, Switzerland. This article is an open access article distributed under the terms and conditions of the Creative Commons Attribution (CC BY) license (<https://creativecommons.org/licenses/by/4.0/>).

## 1. Introduction

In medical [1–4] and computational [5,6] applications, the optical properties of biological tissue, which include the absorption coefficient  $\mu_a$  and the effective scattering coefficient  $\mu'_s$ , are of high interest. We note that the effective scattering coefficient is often more significant for the description of the light propagation in biological media compared to the other two optical scattering quantities involved in radiative transport theory, the scattering phase function  $p(\theta)$  and the single scattering coefficient  $\mu_s$ .

The overall amount of studies for determining the optical properties of biological tissue is relatively large, but the demand in accurate determined properties from the visual (VIS) to the near infrared (NIR) spectral range is still not met due to sparse, inconsistent, sporadic values [7] and not well validated measurement methods. Reviews of publications dealing with the determination of the optical properties of tissue were, e.g., given by Cheong 1990 [8], Kim and Wilson 2011 [9], Sandell and Zhu 2011 [10], Bashkatov et al. 2011 [11] and Jacques 2013 [12]. In the present paper, we mainly refer to recent investigations from Mosca et al. [7] (time and spectral domain) and Foschum [13] (spatial and spectral domain) to compare our results due to their broadband investigations of similar tissue types as were investigated in the present study. Our study is based on an optimized integrating sphere setup having a spectral range from 400 nm to 1400 nm and an innovative two stage evaluation process [14]. The two stage evaluation uses Monte Carlo simulations to describe the exact sample geometry combined with an analytical model that takes the exact sphere geometry into account to correct for the effective detector signal. Thus, the applied theory is based on radiative transfer theory and not on approximations such as Kubelka–Munk theory or diffusion theory. The used optimized integrating sphere was thoroughly verified using polystyrene spheres, Al<sub>2</sub>O<sub>3</sub> and TiO<sub>2</sub> nanoparticles in water and epoxy-based phantoms [15].

In the present paper, we investigated different sample types of the domesticated pig (*sus scrofa domesticus*), which have common genetic elements to primates, are easily acces-

sible and have less pathogenic hazard compared to tissue from primates. In the first part of this paper, we summarize the special features of our novel integrating sphere approach and introduce our sample preparation procedure. The analysis of the influence of an incorrectly assumed refractive index as well as asymmetry factor used for the determination of the optical properties applying an integrating sphere is outlined for adipose tissue in the second part. In the following part of this paper, we present the results of six different tissue types. The results are compared to selected recent literature values, and within this study to different body regions of the same tissue types. Finally, we conclude our results, which may serve as comparison to other setups or investigations.

## 2. Materials and Methods

### 2.1. Experimental Setup and Evaluation Process

An integrating sphere setup combined with advanced Monte Carlo simulations was applied for the accurate separation of  $\mu'_s$  and  $\mu_a$ . The setup and the evaluation procedure were described in detail by Foschum et al. [14] and Bergmann et al. [15] in previous publications. Briefly, we use a halogen lamp as a “white light source”. The light was separated to a reflection, transmission and normalization beam, see Figure 1. The latter was used to correct the measurement for changes in the throughput of the sphere while applying different samples as well as the calibration standard at the sample port. For detection, two commercial available spectrometers with a nominal spectral range from 180 nm to 1100 nm (“Maya2000Pro”, Ocean Insight, Orlando, FL, USA) and from 900 nm to 1700 nm (“NIRQuest512-1.7”, Ocean Insight, Orlando, FL, USA) are connected to two optical fibers. The fiber ends on the north pole of the sphere are imaged onto the sphere wall near the south pole of the sphere. Both spectrometers were corrected for their internal stray light. As a first approximation, we assume that the internal stray light is constant over the entire pixel array [15]. In the VIS, the halogen light source restricted the spectral range to a minimal wavelength of 400 nm, and therefore, we subtracted the internal stray light intensity between 220 nm and 300 nm from each spectrum. For the NIR spectrometer, the internal stray light was considered and corrected by using a short-pass filter in the NIR from 1500 nm to 1585 nm. Due to the large absorption of pure water between 1400 nm to 1500 nm, the evaluated wavelength range was reduced to 400 nm until 1400 nm. The setup is controlled using a self-written C++ software. As mentioned before, we use a two stage evaluation process [14] to solve the inverse problem. This process is based on Monte Carlo simulations to calculate the reflected light from the sample to all parts (port openings and detector field of view) of the integrating sphere. Second, an analytical model of the sphere throughput is used to calculate the effective detector signal after diffusion in the sphere. To enable a fast evaluation of the measurements, look-up tables (LUT) were compiled by performing Monte Carlo simulations of the reflection and transmission from slabs having different effective scattering and absorption coefficients, different thicknesses, different refractive indices, different asymmetry factors and furthermore, considers the refractive index dispersion and the thickness of the cuvette glass [14]. As was stated by Bergmann et al. [15], we constructed and 3D-printed an optimized sphere having an inner diameter of 150 mm. The inner sphere wall was then coated with BaSO<sub>4</sub> by Gigahertz-Optik, Germany. For the evaluation of the biological samples, we used the scattering phase function postulated by Henyey and Greenstein [16] with an asymmetry factor of  $g = 0.9$  and a refractive index of 1.4 surrounded by water, given by Kedenburg et al. [17], and glass (five layers), except for muscle, brain and adipose tissue, for which 1.4 [18] and 1.46 [19] surrounded by glass (three layers, i.e., it is assumed that there are no water layers) were applied, respectively, see Table 1 and Section 2.2.

**Table 1.** Summary of sample types, sample thickness, used refractive index, number of samples (# Samples, 4 repetitions for each sample) and the results of the power law fit, Equation (2) as well as Equation (3) in case of small cylindrical scatterers (in the latter case marked with an \*).

Sample Name	Thickness Range in mm	Refractive Index	# Samples	Power Law Fit, Equations (2) and (3), $a$ as well as $a^*$ in $\text{mm}^{-1}$
non-scalded skin	(1.3–1.9)	5 layers, 1.4	3	$a = 2.1808, b = 0.4912, c = 0.8663$ $a^* = 2.2788, b^* = 0.8317, c^* = 0$
adipose tissue	(2.3–4.1)	3 layers, 1.46 [19]	13	$a = 1.8468, b = 0.0139, c = 0.5953$
muscle	(1.0–3.6)	3 layers, 1.4	11	$a = 0.5798, b = 0.1647, c = 1.1793$
bone cranium	(0.9–1.9)	5 layers, 1.4	4	$a = 1.5963, b = 0.1261, c = 0.5821$
bone mandibula	(0.9–1.4)	5 layers, 1.4	4	$a = 1.9909, b = 0.0417, c = 0.5853$
bone scapula	(1.0–1.4)	5 layers, 1.4	4	$a = 2.0862, b = 0.1008, c = 0.5473$
bone tibia	(0.9–1.0)	5 layers, 1.4	2	$a = 1.9652, b = 0, c = 0.7921$
bone marrow	(2.5–2.6)	5 layers, 1.4	2	$a = 1.2177, b = 0.0475, c = 0.3490$
cartilage	(1.1–1.4)	5 layers, 1.4	3	$a = 2.9583, b = 0.1984, c = 0.9418$ $a^* = 2.9618, b^* = 0.4259, c^* = 0.5777$
brain, white matter	(0.4–2.3)	3 layers, 1.4	6	$a = 8.2925, b = 0, c = 0.8290$
brain, gray matter	(1.0–4.0)	3 layers, 1.4	6	$a = 1.2345, b = 0.0275, c = 1.3291$
dura mater	(1.3–3.5)	5 layers, 1.4	3	$a = 3.8147, b = 0.6265, c = 1.3037$ $a^* = 3.9579, b^* = 0.9605, c^* = 0$
medulla oblongata	(1.4–1.6)	5 layers, 1.4	2	$a = 6.4811, b = 0, c = 0.7731$

## 2.2. Sample Preparation

Besides applying an appropriate experimental setup, also the sample preparation and the measurement procedure are important for a precise determination of the optical properties of tissue. Due to the given measurement apparatus, we are limited to studies that are affected by alterations of the investigated tissue. The tissue preparation may change, e.g., the water content, the oxygenation state and the amount of blood within the tissue [20,21], and therefore the optical properties. Besides this, also freezing-thawing cycles of biological tissues have an influence on the determined optical properties due to cell membrane disruption and liquid loss [7]. Our investigations on gray brain matter of a pig, not shown here, pointed out a relative decrease of around 25% in  $\mu'_s$  and a relative decrease of 5% in  $\mu_a$  at around 550 nm (blood loss) after storing the prepared sample at  $-14^\circ\text{C}$  for 15 days.

In following, we therefore used only fresh samples obtained from the slaughterhouse (Ulmer Fleisch GmbH, Ulm, Germany), prepared and measured within eight hours post-mortem. For organizational reasons of the time consuming preparation process of our samples, a small portion of samples were also stored in the fridge, at  $4^\circ\text{C}$ , for a maximum of two days before measurement. The measurements themselves were performed within two minutes at room temperature, after sample preparation and temperature adjustment. We decided to use the cuvettes mentioned by Bergmann et al. [15] using known N-BK7 glass slides (“34–427”, Edmund Optics, Barrington, NJ, USA) for the measurements, to avoid dehydration, blood loss, surface roughness effects as well as to decrease the influence of the lacking knowledge of the correct refractive indices of the studied tissues. Therefore, we filled liquid with a known refractive index in the space between glass slide and sample surface. This results in a five layered construct surrounded by air, see Figure 1.

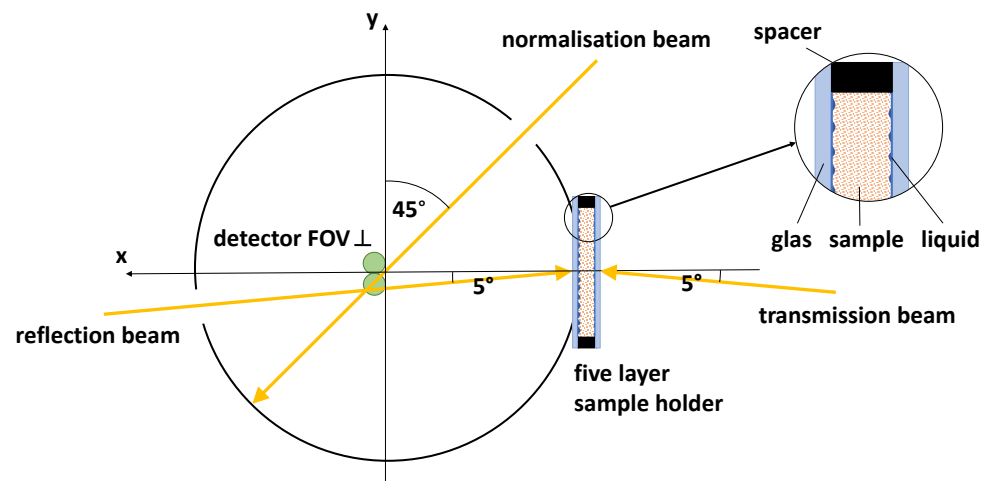


**Figure 1.** Schematic of the used integrating sphere setup in top view including the five layered sample holder. The detector FOV is located perpendicular to the horizontal/equatorial plane near the south pole of the integrating sphere.

The refractive index interfaces are then given by air, glass, liquid, sample, liquid, glass, and air. We used a sodium chloride solution (NaCl 0.9%) as a liquid layer, which has almost the refractive index of water and furthermore enables osmotic balance to prevent further blood loss as well as changes in the tissue structure. The thickness of the liquid layer was assumed to be  $10^{-3}$  mm. For the refractive index of the tissue layer we used  $n = 1.4$ . Varying sample refractive indices in the range of 1.3 to 1.5, which seems to be realistic in biological media [18], results in typical relative changes of the determined effective scattering and absorption coefficients of  $\Delta\mu'_s < 5\%$  and  $\Delta\mu_a < 13\%$ , respectively, according to Monte Carlo simulations. In the case of adipose tissue, muscle and brain matter, the sodium chloride solution was repressed by the soft tissue. Therefore, in the simulation we used a three layered construct with the refractive index value of 1.4 for muscle and brain matter, as well as 1.46 [19] for adipose tissue instead of the five layered construct. Cylindrical spacers were used to enable tissue samples having a defined thickness. For this, we used 3D-printed polylactic acid (PLA) hollow cylinders as well as punched out silicone mats with a sample chamber having a lateral diameter of 30 mm and different axial dimensions. The used silicone mats were applied in case of elastic samples to better control the mechanical stress originating from the glass slides, as, otherwise, there would be a likely change in structural and optical properties. Due to the morphology and constitution of the investigated samples, different preparation methods have been applied. For all the soft tissues like brain matter, dura mater, medulla oblongata and skin, we exclusively used scalpels and tweezers to separate the sample types and in case of dura mater to layer the tissues. For the elastic samples like adipose tissue and muscle, we used a custom made slicer (“universal cutter”, Ritterwerk GmbH, Gröbenzell, Germany), to cut the tissues as plano-parallel as possible. The lateral size was processed with a puncher to produce cylindrical samples with 30 mm in diameter. The harder sample sections of bones were sawed by a saw microtome (“Leica SP1600”, Leica Mikrosysteme Vertrieb GmbH, Wetzlar, Germany). A diamond coated inner-hole saw blade of 280  $\mu\text{m}$  thickness was rotated with 600 rpm and moved with low speed, to obtain plano-parallel samples. Simultaneously, a built-in water cooling device prevented overheating of the saw blade as well as the evaporation of water within the bone tissue. For improved statistics, due to the inhomogeneity of several sample types and to account for the inter-animal variability, repetitions at different lateral positions and different sections as well as different animals were investigated. The maximum thicknesses  $d$  are limited by the transmission signal. Therefore, large absorption coefficients of blood and water in the VIS and NIR spectral range, respectively, obliged us to fabricate smaller sample thicknesses. Sometimes, the sample thicknesses are smaller than needed to achieve

an required optical thickness of  $\tau = \mu'_s d > 2$  [14,15], which is necessary to decrease the influence of the estimated asymmetry factor  $g$  and refractive index  $n$ .

### 2.3. Main Tissue Constituents and Analysis

We compared the obtained absorption spectra with the absorption spectra of the main ingredients, namely de-oxygenated (Hb) and oxygenated (HbO<sub>2</sub>) blood [22], water (VIS [23], NIR [24]), lipid [25] and collagen/elastin [26], see Figure 2. The  $\mu_a$  of collagen, elastin and lipid was obtained from the named literature using the free “WebPlotDigitizer” from Rohatgi [27]. Furthermore, we measured collagen (“hydrolysed bovine collagen”, U Nutrition LTD, Urmston, Greater Manchester, UK), and pork lard (“Schweineschmalz”, LARU, Bottrop, Germany), with the integrating sphere setup to double check the absorption spectra of these tissue types. We found a twofold to threefold larger  $\mu_a$  of collagen compared to the results from Sekar et al. [26] between 1000 nm and 1400 nm, who measured collagen samples in the time domain. We note that in the spectral range of 1150 nm to 1300 nm the absorption peak of collagen as well as elastin have a smaller spectral width compared to that of water. Due to the similarity of the absorption spectra of elastin and collagen in the spectral range from 400 nm to 1400 nm, it is difficult to differentiate between both absorbers. Therefore, in this study, the estimated collagen content is overestimated and could also be caused by elastin. For lipid, we found a good agreement in  $\mu_a$  within the spectral range of 850 nm to 1050 nm, but we obtained a difference by a factor of four at around 600 nm compared to van Veen et al. [25]. The discrepancy in the VIS range could be caused by the difference of the investigated samples. Whereas van Veen et al. used melted fat for the measurements, we used scattering lard at room temperature containing TiO<sub>2</sub> particles. The TiO<sub>2</sub> particles were added to the liquid phase of lard in a previous step by using a hotplate. Furthermore, we measured the melted lard without TiO<sub>2</sub> particles in two separate cuvettes with different thicknesses to validate the measured absorption spectrum. We found a good agreement within our measurements in the range of 420 nm to 1400 nm, whereas the absorption of TiO<sub>2</sub> particles lead to a larger  $\mu_a$  at around 400 nm (data not shown). The refractive index of the liquid phase was measured at 589 nm with an Abbe refractometer (“120709”, Carl Zeiss AG, Oberkochen, Germany) with  $n = 1.464$  and this value as well as the dispersion were measured furthermore with a setup based on the determination of the specular reflection, which was also used in [15] to determine the hemispherical reflectance coefficient of the calibration standard of the integrating sphere. For this measurement, a sample cuvette containing one N-BK7 glass slide, the medium itself and an absorbing backside (black rubber) was used. This was necessary to avoid reflections from the backside. We found a good agreement in the refractive index at 589 nm. The measured dispersion of melted lard can be described by Sellmeier’s equation

$$n(\lambda) = \sqrt{1 + \frac{B_1 \lambda^2}{\lambda^2 - C_1} + \frac{B_2 \lambda^2}{\lambda^2 - C_2} + \frac{B_3 \lambda^2}{\lambda^2 - C_3}} \quad (1)$$

with the coefficients  $B_1 = 1.9496$ ,  $C_1 = 0.0111 \text{ nm}^2$ ,  $B_2 = -0.8303$ ,  $C_2 = 0.0139 \text{ nm}^2$ ,  $B_3 = -1.6134$ ,  $C_3 = -156.5348 \text{ nm}^2$ . For turbid lard at room temperature, we used the same procedure applying the specular reflection measurement and got a dispersion described by Equation (1) with  $B_1 = 1.9613$ ,  $C_1 = 0.0109 \text{ nm}^2$ ,  $B_2 = 0.8168$ ,  $C_2 = 0.0138 \text{ nm}^2$ ,  $B_3 = -1.6358$ ,  $C_3 = -156.9641 \text{ nm}^2$ . At  $\lambda = 589 \text{ nm}$  we obtain  $n = 1.473$ .

The absorption coefficients of pure water and blood from pig were also measured in this study (not shown), resulting in very similar results compared to [22–24]. We note that we did not differ the spectra of oxygenated and de-oxygenated blood from that of oxygenated and de-oxygenated myoglobin.

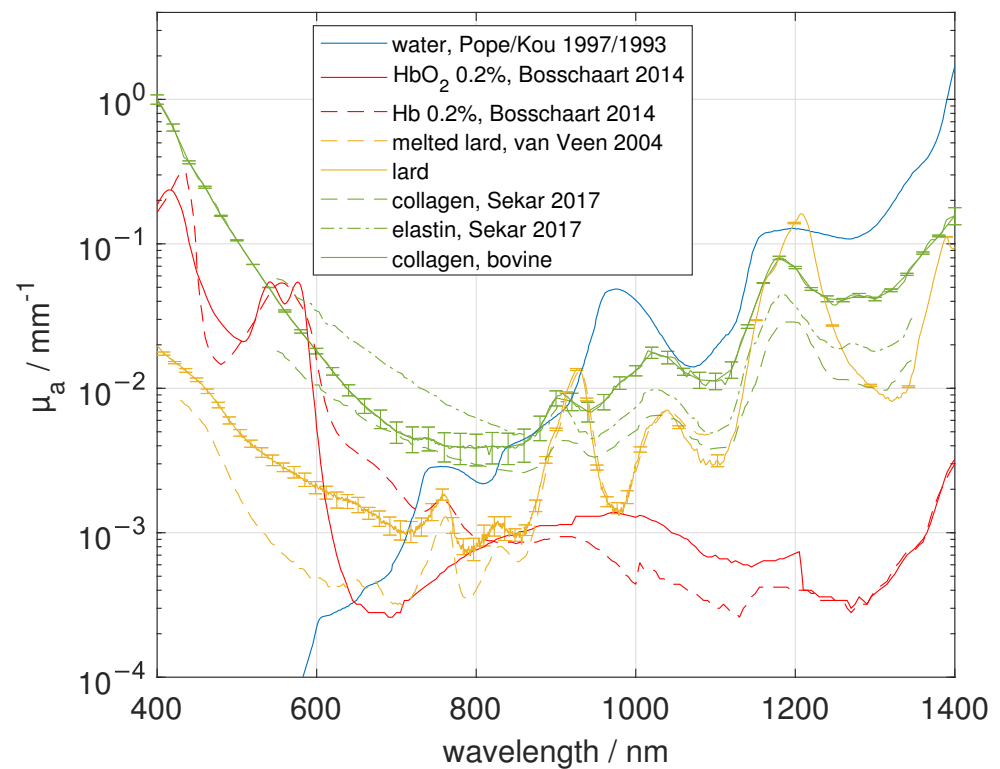


**Figure 2.** Main absorbers in biological tissue adopted from the literature [22–26] or measured within this study.

Besides the absorption coefficient, the effective scattering coefficient is also conclusive for characterizing the investigated tissue. The effective scattering spectra were fitted with two power laws describing two ranges of scattering particle sizes of spherical shape [12,28]

$$\mu'_s(\lambda) = a \cdot (b \cdot (\lambda/\lambda_0)^{-4} + (1 - b) \cdot (\lambda/\lambda_0)^{-c}) \tag{2}$$

with the wavelength  $\lambda$ , the scatter amplitude  $a$ , the fraction of the Rayleigh scatterers  $b$  and the scatter power of the, compared to the wavelength, large scatterers  $c$ . In this study, we used  $\lambda_0 = 630$  nm. The three parameters  $a$ ,  $b$  and  $c$  are related to the density, size and shape of the scatterers in the turbid media. If no Rayleigh scatterers are present, Equation (2) simplifies to the power law containing only the two parameters  $a$  and  $c$  for one range of scattering particle size. If Rayleigh scatterers are present, they contribute more to the scattering in the lower VIS range ( $\lambda^{-4}$  decrease) compared to the longer wavelengths. In most investigated biological tissues, we expect a variety of rather spherical-formed small scatterers and for this it is reasonable to use a generally applicable curve fitting with a  $\lambda^{-4}$  decrease combined with a decrease for larger scatterers using Equation (2). We note that for small cylindrical scatterers, the decrease in  $\mu'_s$  is proportional to  $\lambda^{-3}$  [29]. Therefore, we additionally fitted with

$$\mu'_s(\lambda) = a^* \cdot (b^* \cdot (\lambda/\lambda_0)^{-3} + (1 - b^*) \cdot (\lambda/\lambda_0)^{-c^*}) \tag{3}$$

in case of skin, cartilage and dura mater due to their high content of cylindrically shaped collagen fibrils, see Table 1 as well as Figures 4, 8 and 9 in the following section.

In Table 1, all investigated sample types, sample thicknesses, used refractive indices, number of repetitive measurements (we used samples from a minimum of two animals) as well as the results of the power law fits of the mean  $\mu'_s$  are summarized.

To demonstrate the influence of the applied asymmetry factor and refractive index, we used one sample of adipose tissue (three layered construct) from the back of the pig, having

a sample thickness of 3.5 mm and varied  $g$  as well as  $n$  in the Monte Carlo simulations for fitting the experimental data, see Figure 3. As it was stated by Foschum et al. [14], the impact on the determined optical properties of  $n$  is larger compared to the asymmetry value  $g$ . For example, at 544 nm we obtained a  $\mu'_s = 1.429 \text{ mm}^{-1}$  ( $\tau(\lambda = 544 \text{ nm}) \approx 5$ ) and  $\mu_a = 0.032 \text{ mm}^{-1}$  for the presumed correct optical properties of  $g = 0.9$  and  $n = 1.46$ . A change in  $g$  to 0.75 causes a deviation of 0.24% in  $\mu'_s$  and 0.54% in  $\mu_a$ , whereas a change in  $n$  to 1.4 results in a deviation of 4.76% in  $\mu'_s$  and 14.82% in  $\mu_a$ .

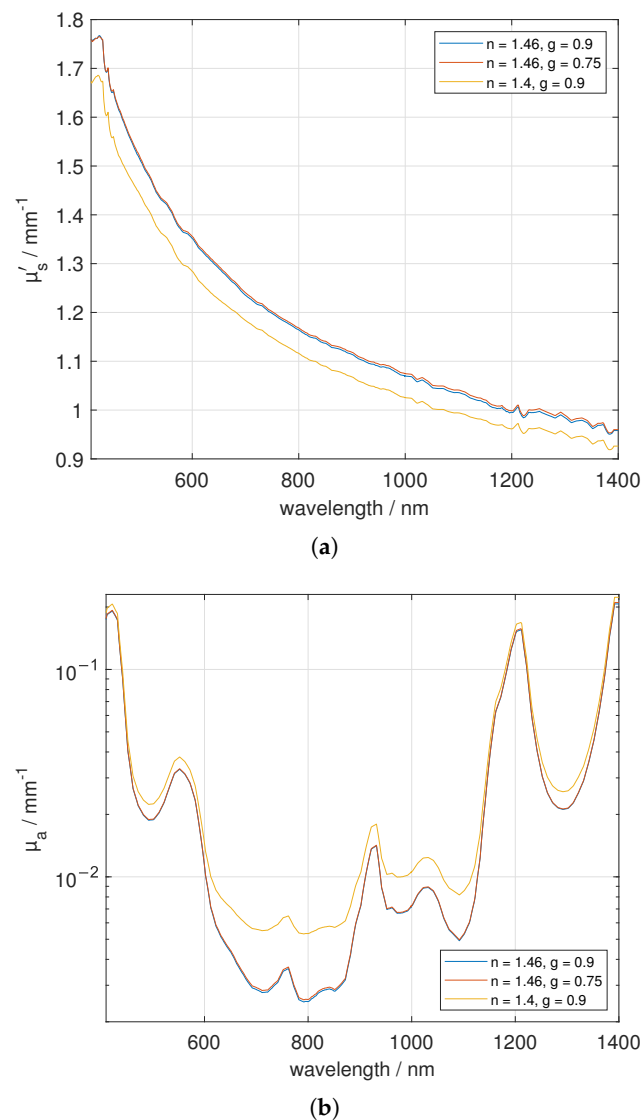


**Figure 3.** Investigation of the impact of  $g$  and  $n$  on adipose tissue (three layered construct) with a sample thickness of 3.5 mm. Figure (a) shows  $\mu'_s$  versus wavelength and (b) depicts  $\mu_a(\lambda)$ .

### 3. Results

#### 3.1. Skin

We investigated fresh, non-scalded skin from the ear of four different animals, preparing in total six samples. First, the hairs were removed with a razor. In the next step, we used a scalpel and a tweezer to separate the skin from the adjacent subcutis, which is mainly composed of connective and adipose tissue. The lateral dimension of the sample was processed by the use of the mentioned puncher with a diameter of 30 mm. Each sample was measured four times by changing the lateral position as well as flipping the sample sides. The samples themselves consist of epidermis and dermis, but were evaluated using a LUT for homogeneous tissue. In Figure 4, the optical properties are given and exemplary

samples, which were prepared for the measurement, are shown under diffuse illumination in reflection and transmission. The skin samples are fairly lateral homogeneous, but a layered structure exists. Regarding the optical properties shown in Figure 4, a strong decrease of  $\mu'_s$  versus wavelength can be seen. We found a good agreement in  $\mu'_s$  between our investigations and the values presented by Mosca et al. [7], who used a stack of five skin specimen for their investigation. Larger standard deviations between 400 nm and 600 nm occur due to the difference in reflection of both sides of the layered specimen (epidermis, dermis as well as a possible small amount of subcutis), especially at larger  $\mu_a$ , where the reflection values are considerably larger than the transmission values. In the skin dermis collagen fibers with diameters of 0.5–8  $\mu\text{m}$  [30] (measured on human neonatal-skin samples), which are dominated by a general orientation parallel to the skin surface, are located. The collagen fibrils of diameters of around 40 nm to 80 nm [31] (measured on bovine and ovine leather), around 100 nm [30] (measured on neonatal-skin samples), or rather in a range of 25 nm to 250 nm [32] (measured on a rat cornea) are positioned in the collagen fibres. Besides the small cylindrical scatterers, a variety of smaller particles and structures exists in the skin dermis which contribute to the Rayleigh scattering of light [30]. Thus, we used both Equations (2) and (3) to fit the measured effective scattering spectra. We found a much larger fraction of Rayleigh scatterers of around 83% assuming small cylindrical scatterers compared to assuming small spherical scatterers, which gives a fraction of around 49%. The subcutis on the other hand consists of connective tissue, adipose tissue, blood vessels and nerves. Therefore, the optical properties of both sample sides are different. As stated before, the smaller particles (collagen fibrils) and structures in the dermis influence more the scattering in the lower VIS (sharp decrease), while larger scatterers (collagen fibres) are dominant in the NIR range. The absorption of skin is mainly influenced by blood (peak around 554 nm), water (peak at about 973 nm) and elastin/collagen (smaller peak-width compared to water at around 1175 nm). The influence of adipose tissue from the subcutis is remarkable small. Unfortunately, it is not easy to separate elastin from collagen absorption spectra, which would be useful as an indicator for dermal skin ageing [33]. Compared to the data presented by Mosca et al. [7], we obtained around two to three times larger  $\mu_a$  in the range of 650 nm to 1100 nm. For this reason, we performed also further investigations on scalded skin samples and found a smaller absorption compared to the non-scalded skin in this range. Furthermore, we found a smaller decrease in  $\mu'_s$  versus wavelength for the scalded skin samples, which may be caused by the treatment at the butchery. The animals were treated with approximately 60 °C water or water vapor (steam scalding) for a few minutes to remove the bristles out of the hair follicles. It can be expected that this treatment will change the collagen structure, the water content, the surface roughness and the elasticity of the sample. In the range of 450 nm to 500 nm, we found an apparent increase of the absorption of the scalded skin, which may be caused by the change of the collagen structure, but could also be induced by the oxygenation of  $\text{Fe}^{2+}$  to  $\text{Fe}^{3+}$  in haemoglobin (methaemoglobin), which increases the absorption in the VIS range between 400 nm and 670 nm, especially at the Soret band at around 405 nm [34]. We notice a double peak for the non-scalded skin around 550 nm, which indicates the oxygenation of hemoglobin. If higher temperatures above 60 °C are applied to skin samples, the destruction of the epidermis [35] and the coagulation of the proteins are expected to increase.



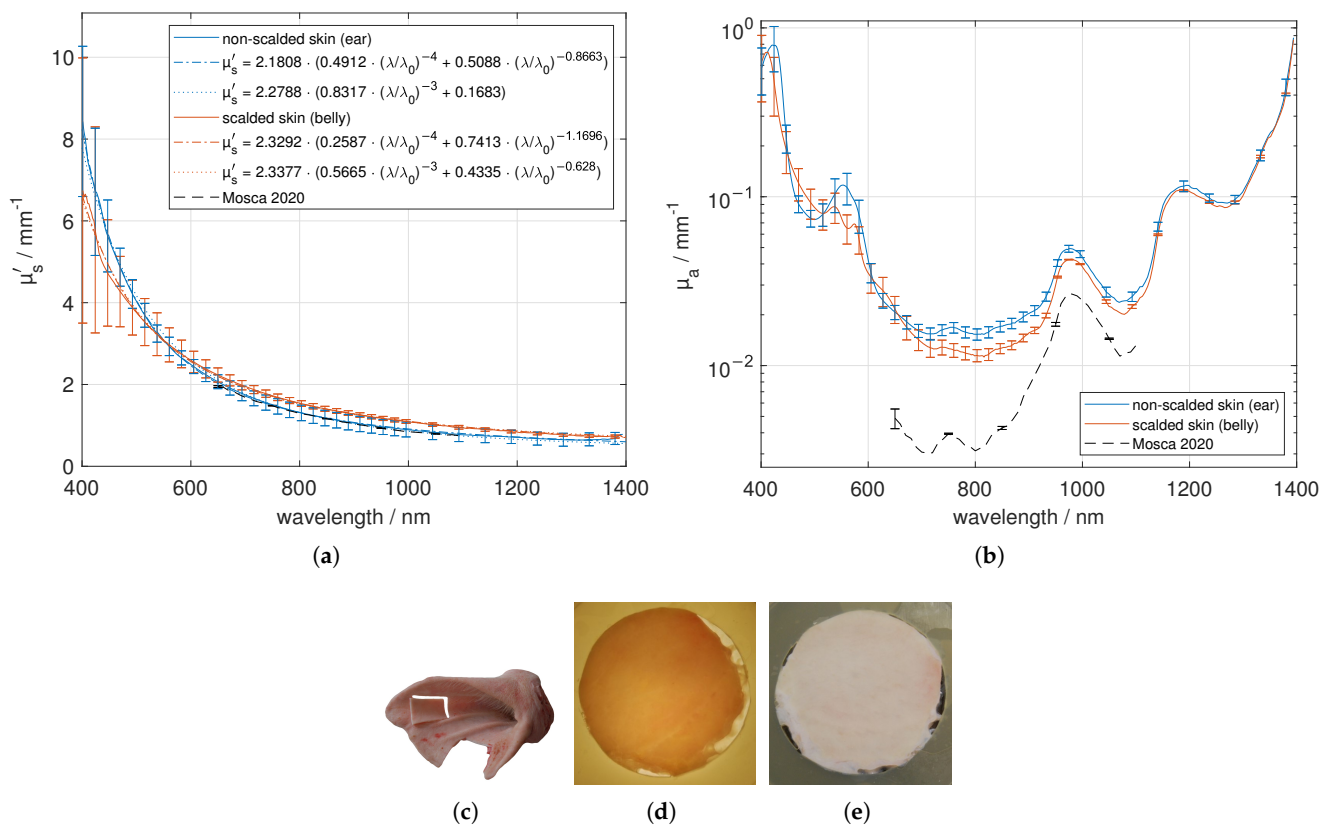


**Figure 4.** Effective scattering coefficient (a) and absorption coefficient (b) versus wavelength for skin. Exemplary tissue sample (c), a 1.46 mm thick sample in transmission (d) and in reflection (e) under diffuse illumination.

### 3.2. Adipose Tissue

The investigated adipose tissues were obtained near the shoulder joint and from the back regions of five pigs. As can be seen in Figure 5c,f, there is a visible intersection within the adipose tissue, and therefore we differentiated between the layer faced to the skin and the layer faced to the muscle. Apart from this, the adipose samples seemed to be fairly homogeneous. We found out that fatty tissue near the skin boundary has a smaller effective scattering coefficient compared to tissue near the muscle boundary (data not shown). Furthermore, adipose tissue near the shoulder joint had a significantly larger  $\mu'_s$  than that from the back (data not shown). The standard deviation of  $\mu'_s$  for a single adipose tissue sample is comparable to the standard deviation from non-scalded skin, compare Section 3.1. In contrast, comparing all measurements of the adipose tissue near the skin and muscle boundary as well as from the shoulder joint and from the back, we obtain a larger standard deviation Figure 5a. Compared to the data presented by Mosca [7] and Foschum [13], we got similar results for  $\mu'_s$  and  $\mu_a$ . In the NIR absorption range the main absorber is fat (in the figure labeled as lard).

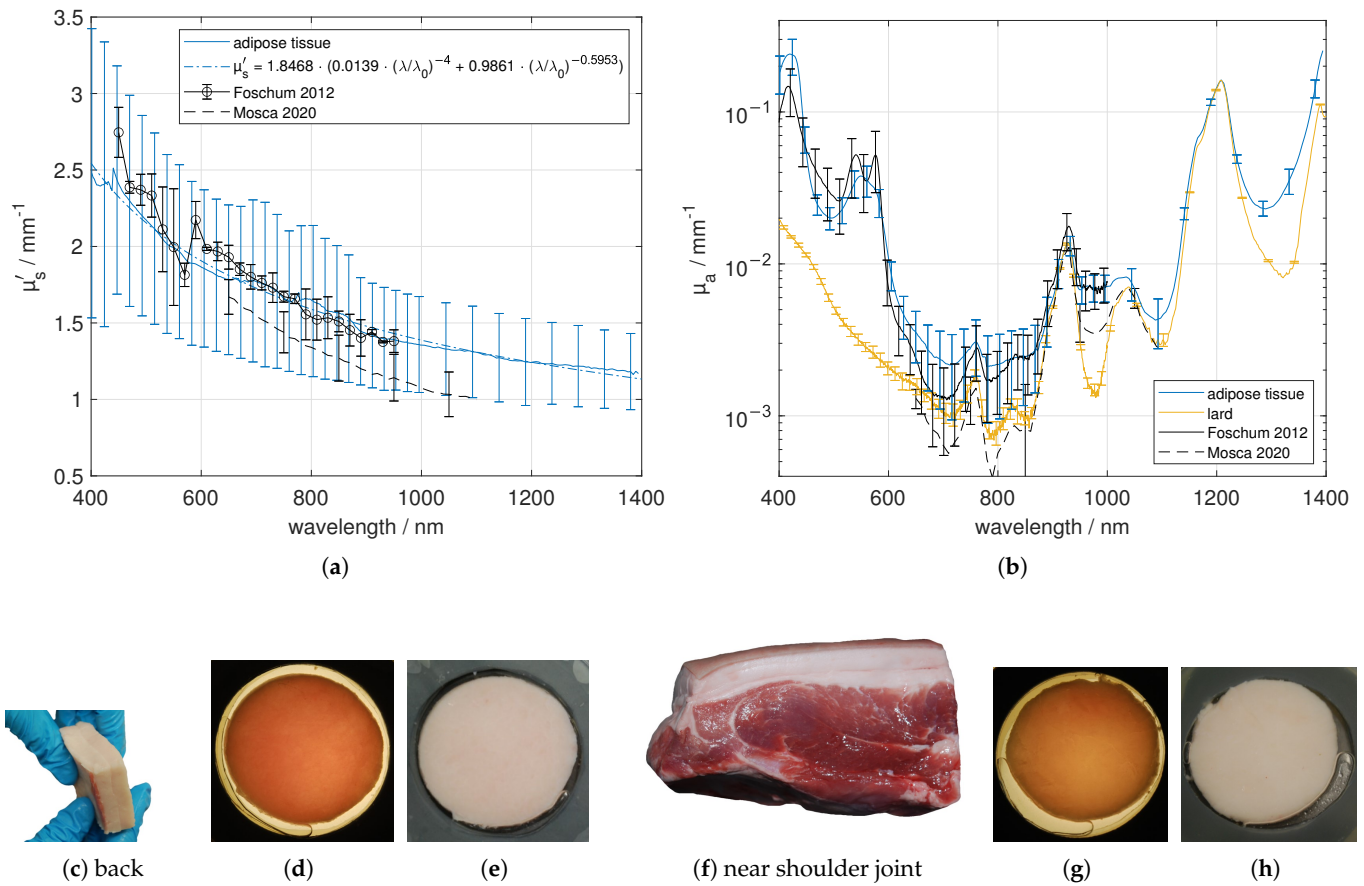


**Figure 5.** Effective scattering coefficient (a) and absorption coefficient (b) versus wavelength for adipose tissue near the shoulder joint and from the back, facing to muscle tissue as well as to skin tissue. Exemplary tissue samples (c,f), a 3.42 mm (back) and a 3.81 mm (near shoulder joint) thick sample in transmission (d,g) and in reflection (e,h) under diffuse illumination.

### 3.3. Muscle

We performed measurements on masticatory muscle and muscle from the shoulder, where it was relatively easy to differentiate the muscle tissue from adjacent tissue. The samples were sliced parallel to the skin layer and therefore parallel to the muscles' longitudinal direction. In Figure 6, the heterogeneous structure caused by the combination of muscle fibers and connective tissue (endomysium/perimysium) is apparent. However, overall the masticatory muscle and the muscle from the shoulder look similar. This was confirmed by the resulting optical properties. The effective scattering is comparable with the mentioned literature values. Further, we found absorption characteristics caused by de-oxygenated blood or rather de-oxygenated myoglobin (around 554 nm [36]), water (around 973 nm) and elastin/collagen (around 1175 nm). As was stated before, we did not differ de-oxygenated blood from de-oxygenated myoglobin. We found a significant difference in the absorption coefficient between 400 nm and 700 nm compared to Foschum [13] and Mosca [7]. Contrary to Foschum [13], we found a larger amount of blood. We note that the light propagation exhibit an anisotropic light propagation caused by the aligned muscle fibers, which was not taken into account in the evaluation process. Thus, the obtained optical properties might strongly depend on the alignment of the muscle fibers relative to the slab surface.

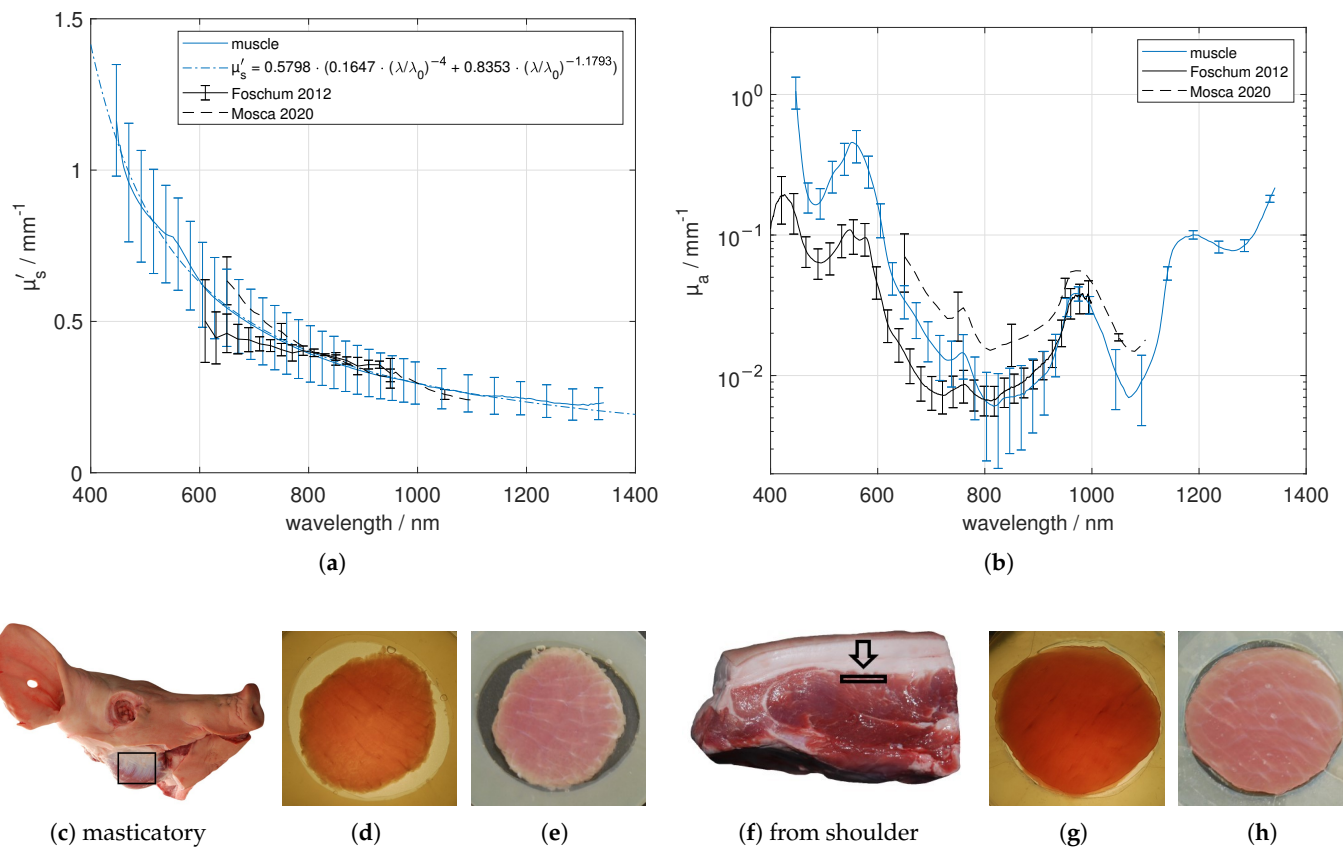


**Figure 6.** Effective scattering coefficient (a) and absorption coefficient (b) versus wavelength for muscle. Exemplary tissue samples (c,f) including region of interest, a 3.53 mm (mastictory muscle) and a 1.86 mm (shoulder) thick sample in transmission (d,g) and in reflection (e,h) under diffuse illumination.

### 3.4. Bone

Several bone samples from the cranium, mandibula, scapula and tibia were investigated. Exemplary sample pictures and determined optical properties are collected in Figure 7. The samples were separated roughly with hammer and chisel or bone saw. We fixed the samples with a two-component resin based on methyl methacrylate plastic ("Technovit 3040", Kulzer GmbH, Hanau, Germany) to saw small parallel slices having thicknesses between 0.9 mm to 1.9 mm using a saw microtome. We mainly investigated the compacta of the bones, which has been cut out parallel to the bone surface as has been illustrated in Figure 7. The saw microtome was cooled with water and after the separation we placed the sample in a closable plastic container filled with sodium chloride solution. This prevents dehydration, which was the main problem of the bone investigation. Dehydrated bone tissue leads to a about five-fold larger  $\mu'_s$ , when dried for 48 h (data not shown). The bone tissues were investigated using the glass plates covering the bone, which was soaked with the sodium chloride solution. The spectral behavior of the effective scattering coefficient was similar for the different bone types, except of that of tibia, which revealed no Rayleigh scattering particles. However, significant differences were found in the absolute values. A good agreement was found with data presented by Mosca et al. [7] and Foschum [13]. Concerning  $\mu_a$  we found absorption characteristics caused by oxygenated blood (double peak at about 540 nm and 577 nm), collagen (shoulder at around 1175 nm in case of scapula and mandibula and a slightly reduced peak-width compared to the case when only a water peak is present), water (around 973 nm) and fat (in case of scapula and mandibula at about 1209 nm). The tibia bone tissue had less blood content. As expected, we found the largest amount of blood in the flat bones, where the bone marrow is producing red corpuscles (haematopoiesis). The absorption coefficient determined by Mosca et al. [7] and Foschum [13] (bone from cow) is within the range of our results. Remarkably, we found

larger differences for the scapula bone samples resulting in a larger standard deviation. For the scapula bone, we found regions with a larger amount of oxygenated blood and less fat content as well as regions with a larger amount of de-oxygenated blood in combination with a larger fat content (data not shown).

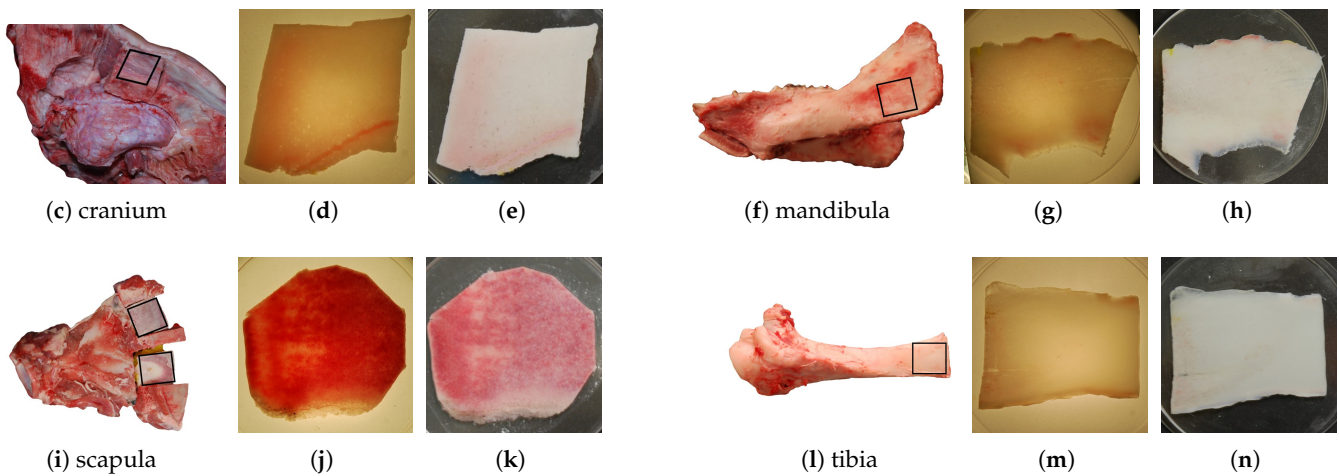
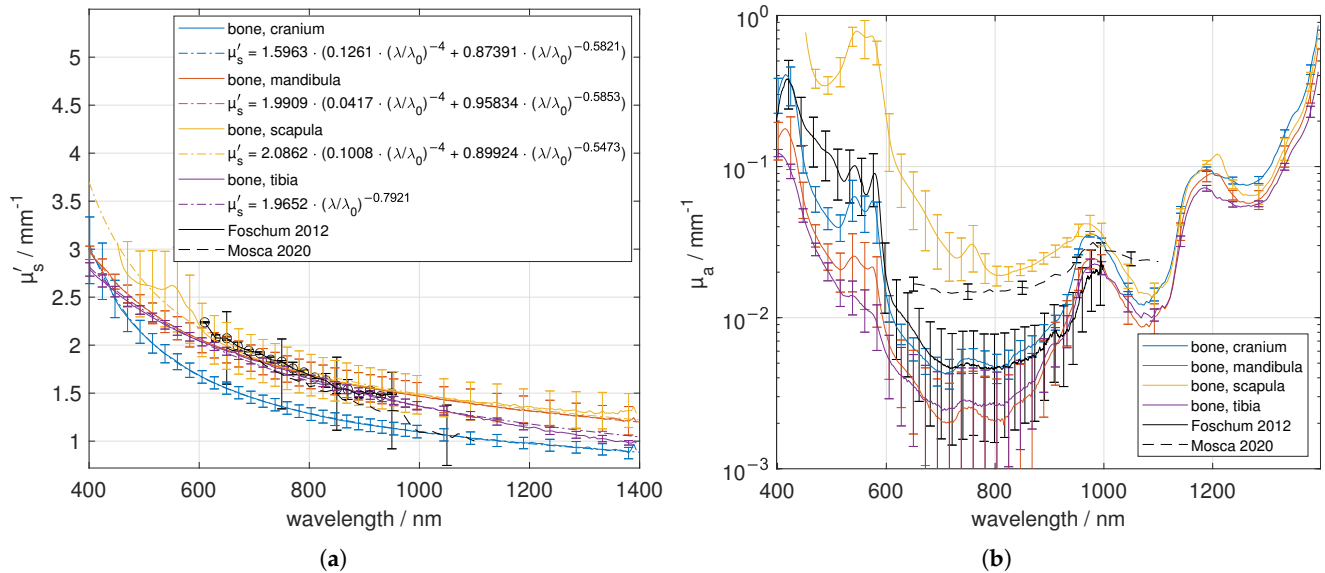


**Figure 7.** Effective scattering coefficient (a) and absorption coefficient (b) versus wavelength for bone. Exemplary tissue samples (c,f,i,l) including region of interest, a 1.05 mm (cranium), a 0.93 mm (mandibula), a 1.33 mm (scapula) and a 0.91 mm (tibia) thick sample in transmission (d,g,j,m) and in reflection (e,h,k,n) under diffuse illumination.

### 3.5. Bone Marrow and Cartilage

Bone marrow from the tibia and elastic cartilage from the ear were investigated by using cuvettes with elastic spacers as described earlier, see Figure 8. Contrary to the cartilage samples, the bone marrow samples look inhomogeneous due to the blood vessels. This results in a larger standard deviation of  $\mu_a$ , especially between 450 nm and 600 nm. The elastic cartilage was separated from the non-scalded skin of the ears. For the elastic cartilage, the sharp decrease in  $\mu'_s$  versus wavelength is caused by the collagen fibrils due to their small diameter compared to the wavelength of the applied light. Again, applying Equation (3) results in a larger fraction of Rayleigh scatterers of around 43% compared to the use of Equation (2), resulting in 20%. Comparing the absorbers from Figure 2, we found absorption characteristics based on oxygenated blood (double peak at about 540 nm and 577 nm), fat (about 1209 nm) and elastin/collagen (shoulder at about 1175 nm) for bone

marrow and absorption based on water (around 973 nm) and collagen (slightly reduced peak-width compared to water around 1175 nm) for the cartilage sample.

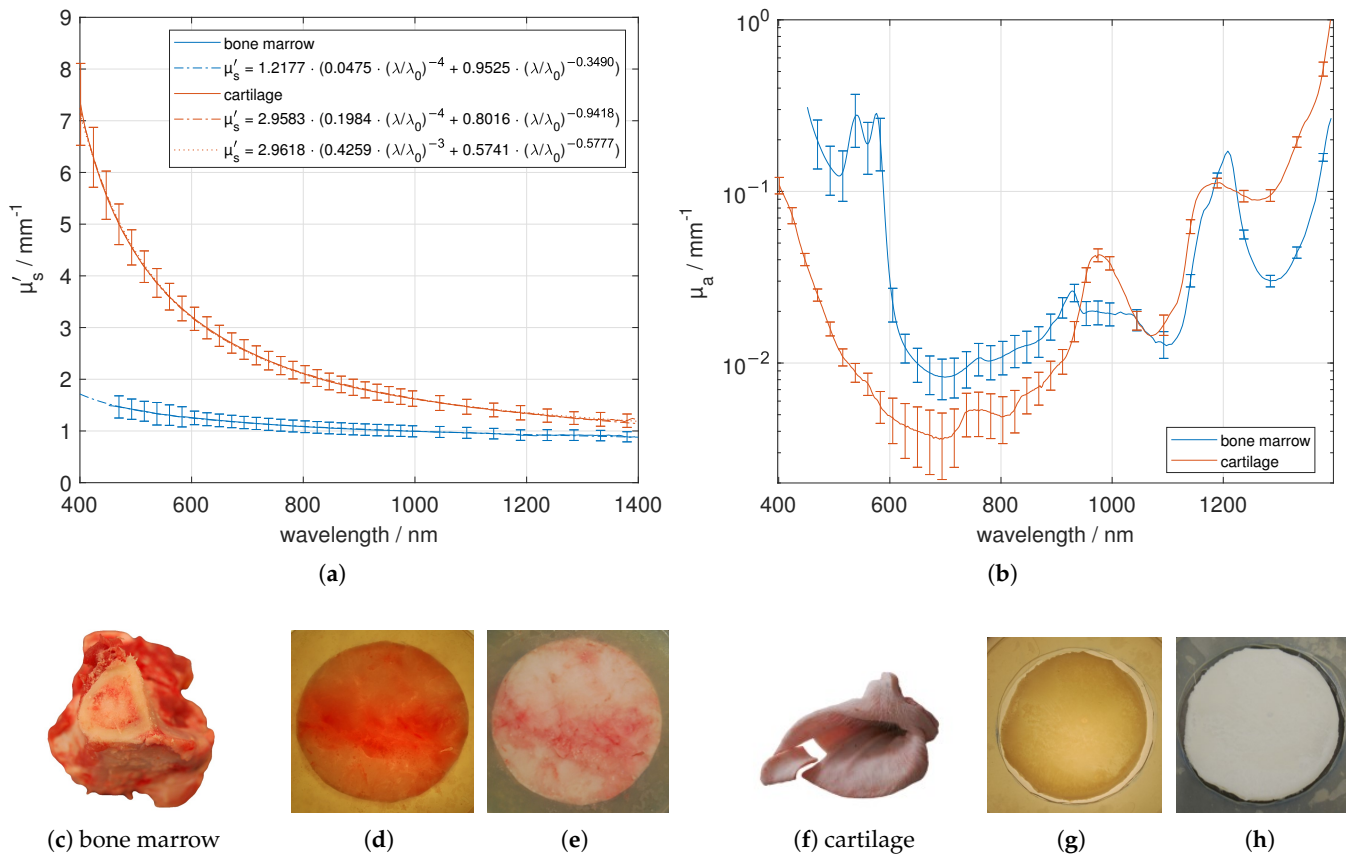


**Figure 8.** Effective scattering coefficient (a) and absorption coefficient (b) versus wavelength for bone marrow and cartilage. Exemplary tissue samples (c,f), a 2.54 mm (bone marrow) and a 1.12 mm (elastic cartilage) thick sample in transmission (d,g) and in reflection (e,h) under diffuse illumination.

### 3.6. Brain

We obtained three different fresh brains and prepared six samples of gray (substantia grisea) and white (substantia alba) brain matter out of it. The separation of white and gray matter was done with scalpel and tweezers. Larger regions of white brain matter were found at the bottom of the brain, and adjacent on the inner side of the cortex. The gray brain matter was separated from the inner white matter. Especially for the gray brain matter, see Figure 9, several pieces were butt-jointed. The resulted samples looked more or less inhomogeneous due to impurities from adjacent tissue. In addition, we investigated the dura mater as a stack of thin layers and the medulla oblongata, which we gathered from two fresh pig heads by separating the skull from the inside organ using hammer and chisel. Both, the dura mater and the medulla oblongata samples looked homogeneous. The obtained effective scattering of white matter was much larger compared to the effective scattering of gray brain. For example, at 633 nm, we found a difference by a factor of about seven. The white brain matter had less blood and a larger amount of water and fat compared to the gray brain matter. The larger  $\mu'_s$  of the white brain matter compared to gray brain matter is the main reason for its whitish appearance. Comparing the results of the brain tissues with the data presented by Mosca et al. [7], we found a better agreement for  $\mu_a$  than for  $\mu'_s$ . The difference of the  $\mu'_s$  values presented by Mosca et al. compared to our results depends again on the difference in the investigated sample. Whereas our samples were separated into the mentioned constituents, Mosca et al. measured the optical properties from the whole brain including gray and white brain matter. The pronounced decrease of  $\mu'_s$  for the dura mater in the lower VIS spectral range is dominated by the

small substituents like collagen fibrils. Therefore we recommend to use Equation (3) for the description of the sharp decrease in  $\mu'_s$ , which gives an amount of around 96% of Rayleigh scatterers compared to the assumption of spherical scatterers, which results in approximately 63% of Rayleigh scatterers. We found absorption characteristics based on de-oxygenated blood (around 554 nm), water (around 973 nm), collagen (indicated by a slightly reduced peak width compared to the case when only a water peak is present) and fat (peak at about 1209 nm for medulla oblongata and white brain matter).

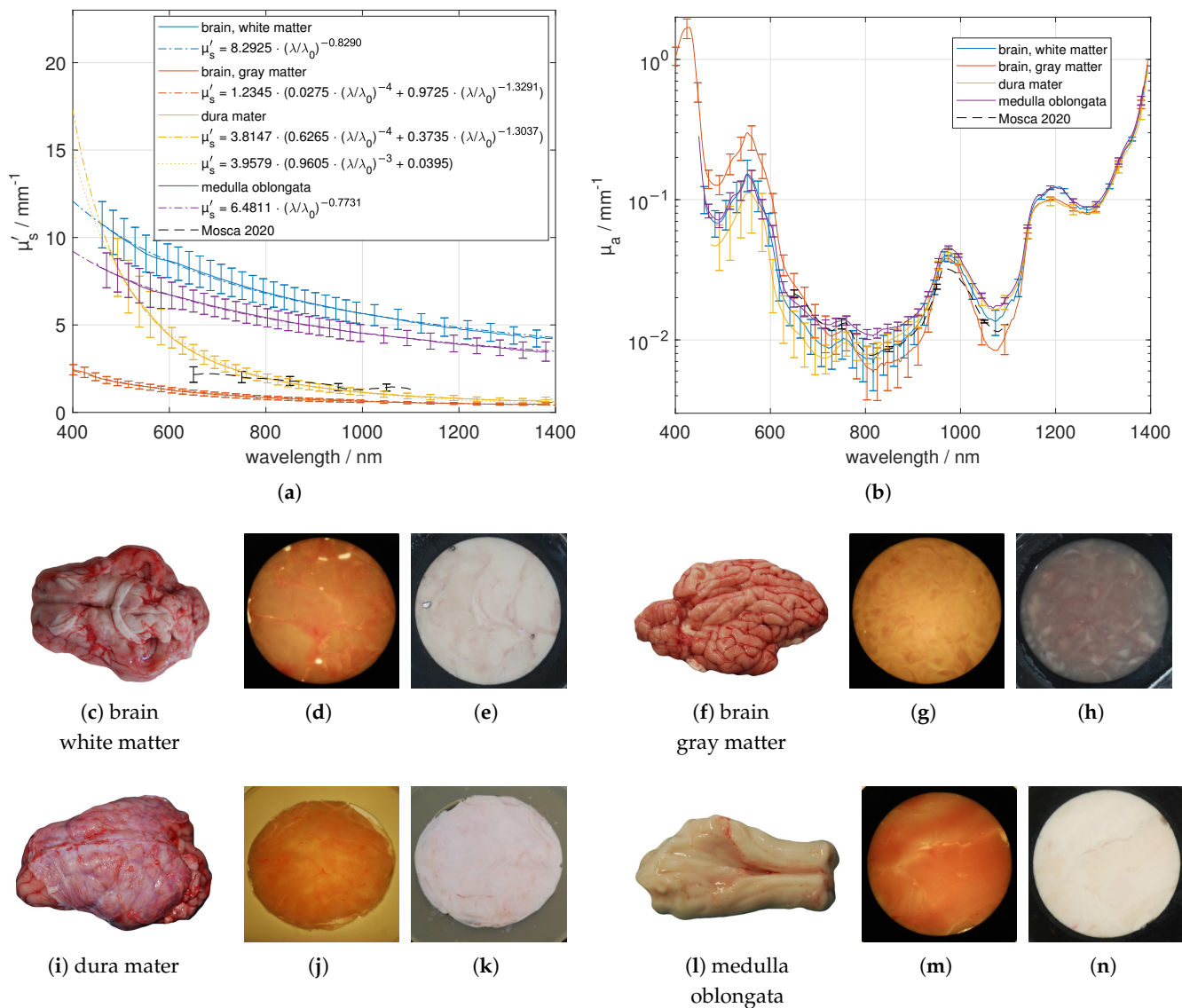


**Figure 9.** Effective scattering coefficient (a) and absorption coefficient (b) versus wavelength for brain tissue. Exemplary tissue samples (c,f,i,l), a 1.03 mm (white brain matter), a 1.06 mm (gray brain matter), a 1.37 mm (dura mater) and a 1.54 mm (medulla oblongata) thick sample in transmission (d,g,j,m) and in reflection (e,h,k,n) under diffuse illumination.

### 3.7. Quantitative Study

We quantitatively analyzed the concentration of the mentioned main absorbers water, fat, collagen, de-oxygenated blood and oxygenated blood using the obtained mean absorption spectra of each tissue type. To this aim, nonlinear regressions (“lsqcurvefit” using MATLAB R2020a, MathWorks, Natick, MA, USA) to the logarithmized data of the obtained absorption spectra for each tissue type were performed for wavelengths from 400 nm to 1400 nm using equal weights. We used the mean absorption spectra of water, oxygenated blood and de-oxygenated blood from the mentioned literature [22–24] and fat as well

as collagen from our own measurements. Fitting parameters were the concentrations of the main absorbers and a spectral constant offset. The latter was introduced due to the presence of further absorbing substituent besides the main absorbers. For the average sum of the main absorber's concentrations we obtain 85.35%, reaching from 62.45% for muscle to 105.22% for bone marrow. These values may be influenced by systematic errors like possibly incorrect absorption spectra of the main absorbers or of the measured mean absorption spectra of the tissue types, for example due to inhomogeneous samples, the similarity in the absorption spectra, for example between water and collagen in the NIR spectral range, or by another, not regarded main absorber, which may be present in the tissue. The obtained results are given in Figure 10 and listed in Table 2. In general, we found a good agreement between the derived absorption spectra and the fitted spectra using the nonlinear regression for non-scalded skin, adipose tissue, bone cranium, bone mandibula, bone scapula, bone tibia, bone marrow, elastic cartilage, brain white matter and dura mater. To quantify the remaining deviation between the measured absorption spectra  $\mu_a$  and the absorption spectra determined by the fit algorithm  $\mu_{a,fit}$ , we used

$$E = \frac{1}{N-P} \sum_{i=1}^N \left( \frac{\mu_{a,fit,i} - \mu_{a,i}}{\Delta\mu_{a,i}} \right)^2, \quad (4)$$

with the total number  $N$  of 354 spectral values  $i$ ,  $P = 6$ , the number of parameters of the fit model and the standard deviation of the measured absorption spectra  $\Delta\mu_a$  [37]. For most of the investigated tissues we received  $E < 1$  due to the large standard deviation of the measured absorption spectra. Only for muscle ( $E = 1.087$ ), brain gray matter ( $E = 1.403$ ) and medulla oblongata ( $E = 1.831$ ) we obtained a larger discrepancy of the measured spectral absorption using the fit model. For non-scalded skin, we obtained concentrations of 66.31% water, 3.11% fat, 24.36% collagen, 0.32% de-oxygenated blood and 0.05% oxygenated blood. The fat content may be influenced from the subcutis, which was not easy to separate from the skin. Due to further not considered absorbers, we obtained a constant offset factor of  $0.012 \text{ mm}^{-1}$ . In adipose tissue we found a pure fat content of 82.21%, which seems to be realistic. For the fit of the spectral absorption of the adipose tissue, no additional offset factor was necessary. In muscle, we found a concentration of 59.25% water, 0% fat, 1.55% collagen and 1.65% de-oxygenated blood. In muscle tissue collagen can be found in the connective tissue and in tendons. Unfortunately, the similarity in  $\mu_a$  between water and collagen in the NIR spectral range can affect the obtained absolute values of the water and collagen concentration, especially for larger  $E$ . For bone and related tissue we found a large variety of the concentrations of the main absorbers. We found a water content between 38.73% and 61.58%, a fat content between 1.5% and 31.68% and a collagen content between 0% and 17.92%. We mention that the results of Taroni et al. [38] are comparable to our results for the bone tissue composition. Taroni et al. estimated a content of 41.2% for water, 20.3% for fat, 18% for collagen, 2% for de-oxygenated blood and 2.3% for oxygenated blood. In our measurements of the scapula bone tissue we found 2.98% of de-oxygenated and 0.53% of oxygenated blood. As stated before, due to haematopoiesis we expected a higher amount of blood in the flat bones. Bone marrow showed a large fat content and a large content of oxygenated blood, the latter is necessary for the supply of the brain. Cartilage is mainly composed of water and collagen, whereas the collagen content obtained in this study is smaller than expected. For brain and related tissue we found again a large variety, depending on the function of the tissue. We found an approximately twofold larger de-oxygenated blood content of the gray brain matter compared to the white brain matter. Rejmstad et al. [39] estimated an oxygen saturation in the white (24%) and gray (52%) human brain tissue. However, in our study, the de-oxygenated blood content of the white brain matter was comparable to the medulla oblongata, which was extracted beneath the brain cortex. We note that we used cuvettes for the sample measurement with sodium chloride solution between tissue and glass slide. Thus, this additional layer, which was regarded in the evaluation with refractive index and assumed thickness, may lead to a larger water content than is expected in physiological conditions. Overall, we estimate a

relative error of around 10% for the determined concentrations of absorbers having a large volume fraction. This error is, e.g., due to the assumption of a homogeneous model, which neglects the inhomogeneity of the scattering and absorbing structures of the considered samples, the simplified assumptions concerning the refractive index, and the uncertainty in the absorption spectra of the main absorbers. Finally, we note that our results were obtained from fresh samples. Compared to measurements, the results of our measurements differ, especially the water, oxygenated and de-oxygenated blood content will be affected.

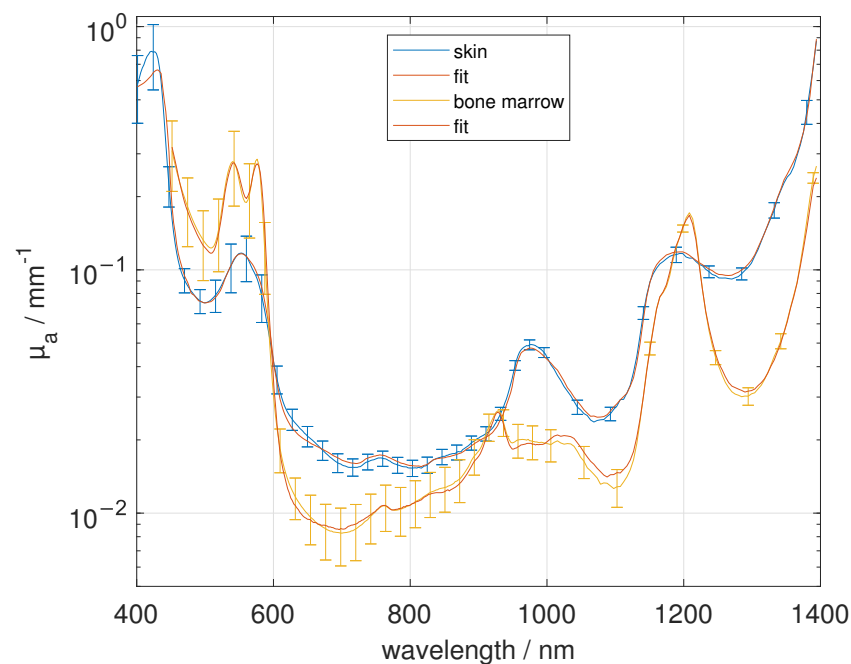


**Figure 10.** Comparison of the absorption spectra from 400 nm to 1400 nm of skin and bone marrow with the fitted concentrations of water, fat, collagen, de-oxygenated blood and oxygenated blood and a constant offset factor.

**Table 2.** Summary of the analyzed concentrations of the mentioned main absorbers water, fat, collagen, de-oxygenated blood and oxygenated blood, the spectral constant offset and *E*, Equation (4).

Sample Name	Water in %	Fat in %	Collagen in %	Hb Blood in %	HbO <sub>2</sub> Blood in %	Constant $\mu_a$ in $\text{mm}^{-1}$	<i>E</i>
non-scalded skin	66.31	3.11	24.36	0.32	0.05	0.012	0.29
adipose tissue	10.29	82.21	1.6	0.09	0.05	0	0.266
muscle	59.25	0	1.55	1.65	0	0	1.087
bone cranium	61.58	1.5	17.92	0.09	0.1	0.002	0.346
bone mandibula	43.01	20.24	13.95	0.07	0	0	0.108
bone scapula	48.63	31.68	0	2.98	0.53	0.002	0.382
bone tibia	38.73	11.82	12.43	0.02	0	0.001	0.642
bone marrow	9.96	88.97	5.31	0	0.97	0.006	0.145
cartilage	79.61	3.47	10.72	0	0	0.003	0.155
brain, white matter	67.24	17.18	14.3	0.56	0	0.003	0.222
brain, gray matter	63.47	0	11.82	1.22	0	0	1.403
dura mater	70.27	5.4	6.07	0.33	0.07	0.004	0.284
medulla oblongata	69.55	8.69	17.62	0.54	0	0.006	1.831

#### 4. Conclusions

In this study, an integrating sphere setup was used in the wavelength range between 400 nm to 1400 nm, in combination with an innovative two stage evaluation process, to



investigate the intrinsic optical properties  $\mu'_s$  and  $\mu_a$  of porcine samples. In more detail, we investigated various tissue types (skin, muscle, adipose tissue, bone, cartilage, brain) from different individual animals as well as from different sections. However, this study has some limitations as we could not perform measurements due to the used setup. Therefore, e.g., the oxygenation of blood, the amount of blood and water within the tissue and the tissue microstructure could have been changed and, thus, altered the optical properties. In order to reduce this, we exclusively used cuvettes filled with sodium chloride solution and measured the samples postmortem within eight hours. The decrease in  $\mu'_s$  was described by two different laws consisting of two combined power laws applicable for rather spherical or cylindrical scatterers. For biological tissue containing small cylindrical scatterers like collagen fibrils in skin, cartilage and dura mater we found a nearly twofold larger amount of Rayleigh scatterers when small cylindrical scatterers compared to small spherical scatterers are assumed. All tissue types show characteristic peaks in  $\mu_a$ , corresponding to blood, water, lipid, collagen and elastin. Due to the large standard deviation of the measured absorption spectra, we quantitatively estimated the constituents mostly with  $E < 1$  between the measured and the fitted absorption spectra. However, we note that in this study it was assumed that the considered tissue samples are homogeneous, which is not always a good approximation, especially for muscle, bone marrow and brain tissue. We compared the resulted tissue optical properties with two selected publications that measured similar porcine tissue types in a relatively large spectral range and found, in general, a good agreement. This is remarkable, since we compared measurements using different measurement principles. Our results can be used, e.g., in the medical field to predict the light distribution in tissue and therewith to calculate the penetration depths, fluence rate distributions or to interpret measurement signals, like the reflection and transmission from investigated biological tissue. Furthermore, the results can help to improve digital visualization of biological tissue using physics based rendering and to construct realistic tissue phantoms.

**Author Contributions:** Conceptualization, F.B., F.F. and A.K.; methodology, F.B.; software, F.B. and F.F.; validation, F.B. and F.F.; formal analysis, F.B.; investigation, F.B. and L.M.; resources, A.K.; data curation, F.B.; writing—original draft preparation, F.B.; writing—review and editing, F.B., F.F. and A.K.; visualization, F.B.; supervision, A.K.; project administration, F.B. All authors have read and agreed to the published version of the manuscript.

**Funding:** This research received no external funding.

**Data Availability Statement:** The data presented in this study are openly available and can be found here: <https://www.ilm-ulm.de/publikationen-1-1.html>.

**Acknowledgments:** We acknowledge the Ulmer Fleisch GmbH for their cooperativeness.

**Conflicts of Interest:** The authors declare that there are no conflict of interest related to this article.

## References

1. Fantini, S.; Walker, S.A.; Franceschini, M.A.; Kaschke, M.; Schlag, P.M.; Moesta, K.T. Assessment of the size, position, and optical properties of breast tumors by noninvasive optical methods. *Appl. Opt.* **1998**, *37*, 1982–1989. [[CrossRef](#)] [[PubMed](#)]
2. Tromberg, B.J.; Shah, N.; Lanning, R.; Cerussi, A.; Espinoza, J.; Pham, T.; Svaasand, L.; Butler, J. Non-invasive characterization of breast tumors using photon migration spectroscopy. *Neoplasia* **2000**, *2*, 26–40. [[CrossRef](#)]
3. Ritz, J.P.; Roggan, A.; Isbert, C.; Müller, G.; Buhr, H.J.; Germer, C.T. Optical properties of native and coagulated porcine liver tissue between 400 and 2400 nm. *Lasers Surg. Med. Off. J. Am. Soc. Laser Med. Surg.* **2001**, *29*, 205–212. [[CrossRef](#)] [[PubMed](#)]
4. Vahrmeijer, A.L.; Frangioni, J.V. Seeing the invisible during surgery. *Br. J. Surg.* **2011**, *98*, 749. [[CrossRef](#)] [[PubMed](#)]
5. Jensen, H.W.; Marschner, S.R.; Levoy, M.; Hanrahan, P. A practical model for subsurface light transport. In Proceedings of the ACM SIGGRAPH, New York, NY, USA, 1 August 2001; pp. 511–518
6. Zoller, C.J.; Hohmann, A.; Forchum, F.; Geiger, S.; Geiger, M.; Ertl, T.P.; Kienle, A. Parallelized Monte Carlo software to efficiently simulate the light propagation in arbitrarily shaped objects and aligned scattering media. *J. Biomed. Opt.* **2018**, *23*, 065004. [[CrossRef](#)] [[PubMed](#)]
7. Mosca, S.; Lanka, P.; Stone, N.; Sekar, S.K.V.; Matousek, P.; Valentini, G.; Pifferi, A. Optical characterization of porcine tissues from various organs in the 650–1100 nm range using time-domain diffuse spectroscopy. *Biomed. Opt. Express* **2020**, *11*, 1697–1706. [[CrossRef](#)] [[PubMed](#)]

8. Cheong, W.F.; Prahl, S.A.; Welch, A.J. A review of the optical properties of biological tissues. *IEEE J. Quantum Electron.* **1990**, *26*, 2166–2185. [[CrossRef](#)]
9. Kim, A.; Wilson, B.C. Measurement of and tissue optical properties: Methods and theories. In *Optical-Thermal Response of Laser-Irradiated Tissue*; Springer: Berlin/Heidelberg, Germany, 2010; pp. 267–319.
10. Sandell, J.L.; Zhu, T.C. A review of optical properties of human tissues and its impact on PDT. *J. Biophotonics* **2011**, *4*, 773–787. [[CrossRef](#)]
11. Bashkatov, A.N.; Genina, E.A.; Tuchin, V.V. Optical properties of skin, subcutaneous, and muscle tissues: A review. *J. Innov. Opt. Health Sci.* **2011**, *4*, 9–38. [[CrossRef](#)]
12. Jacques, S.L. Optical properties of biological tissues: A review. *Phys. Med. Biol.* **2013**, *58*, R37. [[CrossRef](#)]
13. Foschum, F. Bestimmung der Optischen Eigenschaften Trüber Medien Mittels Nichtinvasiver Remissionsmessungen. Ph.D. Thesis, Fakultät für Naturwissenschaften, Universität Ulm, Ulm, German, 2012.
14. Foschum, F.; Bergmann, F.; Kienle, A. Precise determination of the optical properties of turbid media using an optimized integrating sphere and advanced Monte Carlo simulations. Part 1: Theory. *Appl. Opt.* **2020**, *59*, 3203–3215. [[CrossRef](#)] [[PubMed](#)]
15. Bergmann, F.; Foschum, F.; Zuber, R.; Kienle, A. Precise determination of the optical properties of turbid media using an optimized integrating sphere and advanced Monte Carlo simulations. Part 2: Experiments. *Appl. Opt.* **2020**, *59*, 3216–3226. [[CrossRef](#)] [[PubMed](#)]
16. Henyey, L.G.; Greenstein, J.L. Diffuse radiation in the galaxy. *Astrophys. J.* **1941**, *93*, 70–83. [[CrossRef](#)]
17. Kedenburg, S.; Vieweg, M.; Gissibl, T.; Giessen, H. Linear refractive index and absorption measurements of nonlinear optical liquids in the visible and near-infrared spectral region. *Opt. Mater. Express* **2012**, *2*, 1588–1611. [[CrossRef](#)]
18. Khan, R.; Gul, B.; Khan, S.; Nisar, H.; Ahmad, I. Refractive index of biological tissues: Review, measurement techniques, and applications. *Photodiagnosis Photodyn. Ther.* **2021**, *33*, 102192.
19. Shahidi, F. *Bailey's Industrial Oil and Fat Products, Edible Oil and Fat Products: Processing Technologies*; John Wiley & Sons: Hoboken, NJ, USA, 2005; Volume 5.
20. Doiron, D.R.; Svaasand, L.O.; Profio, A.E. Light dosimetry in tissue: Application to photoradiation therapy. *Porphy. Photosensit.* **1983**, *160*, 63–76.
21. Wilson, B.C.; Jeeves, W.P.; Lowe, D.M. In vivo and post mortem measurements of the attenuation spectra of light in mammalian tissues. *Photochem. Photobiol.* **1985**, *42*, 153–162. [[CrossRef](#)] [[PubMed](#)]
22. Bosschaart, N.; Edelman, G.J.; Aalders, M.C.; van Leeuwen, T.G.; Faber, D.J. A literature review and novel theoretical approach on the optical properties of whole blood. *Lasers Med. Sci.* **2014**, *29*, 453–479.
23. Pope, R.M.; Fry, E.S. Absorption spectrum (380–700 nm) of pure water. II. Integrating cavity measurements. *Appl. Opt.* **1997**, *36*, 8710–8723. [[CrossRef](#)]
24. Kou, L.; Labrie, D.; Chylek, P. Refractive indices of water and ice in the 0.65-to 2.5- $\mu\text{m}$  spectral range. *Appl. Opt.* **1993**, *32*, 3531–3540. [[CrossRef](#)]
25. Van Veen, R.; Sterenborg, H.J.; Pifferi, A.; Torricelli, A.; Chikoidze, E.; Cubeddu, R. Determination of visible near-IR absorption coefficients of mammalian fat using time- and spatially resolved diffuse reflectance and transmission spectroscopy. *J. Biomed. Opt.* **2005**, *10*, 054004. [[CrossRef](#)]
26. Sekar, S.K.V.; Beh, J.S.; Farina, A.; Dalla Mora, A.; Pifferi, A.; Taroni, P. Broadband diffuse optical characterization of elastin for biomedical applications. *Biophys. Chem.* **2017**, *229*, 130–134. [[CrossRef](#)]
27. Rohatgi, A. WebPlotDigitizer. 2020. Available online: <https://automeris.io/WebPlotDigitizer/> (accessed on 28 January 2021)
28. Graaff, R.; Aarnoudse, J.; Zijp, J.R.; Sloot, P.; De Mul, F.; Greve, J.; Koelink, M. Reduced light-scattering properties for mixtures of spherical particles: A simple approximation derived from Mie calculations. *Appl. Opt.* **1992**, *31*, 1370–1376. [[CrossRef](#)]
29. Bohren, C.F.; Huffman, D.R. *Absorption and Scattering of Light by Small Particles*; John Wiley & Sons: Hoboken, NJ, USA, 2008.
30. Saidi, I.S.; Jacques, S.L.; Tittel, F.K. Mie and Rayleigh modeling of visible-light scattering in neonatal skin. *Appl. Opt.* **1995**, *34*, 7410–7418. [[CrossRef](#)]
31. Wells, H.C.; Edmonds, R.L.; Kirby, N.; Hawley, A.; Mudie, S.T.; Haverkamp, R.G. Collagen fibril diameter and leather strength. *J. Agric. Food Chem.* **2013**, *61*, 11524–11531. [[CrossRef](#)]
32. Bancelin, S.; Aimé, C.; Gusachenko, I.; Kowalczyk, L.; Latour, G.; Coradin, T.; Schanne-Klein, M.C. Determination of collagen fibril size via absolute measurements of second-harmonic generation signals. *Nat. Commun.* **2014**, *5*, 4920. [[CrossRef](#)]
33. Puschmann, S.; Rahn, C.D.; Wenck, H.; Gallinat, S.; Fischer, F.F. Approach to quantify human dermal skin aging using multiphoton laser scanning microscopy. *J. Biomed. Opt.* **2012**, *17*, 036005. [[CrossRef](#)] [[PubMed](#)]
34. Martínez-Mancera, F.D.; Hernández-López, J.L. In vitro observation of direct electron transfer of human haemoglobin molecules on glass/tin-doped indium oxide electrodes. *J. Mex. Chem. Soc.* **2015**, *59*, 302–307.
35. Worlicek, C. Fluoreszenzinduktion und Relatives Penetrationsverhalten Verschiedener 5-Aminolävulinsäure/-Methylester Formulierungen am Ex-Vivo Schweinehautmodell. Ph.D. Thesis, Medizinische Fakultät, Universität Regensburg, Regensburg, Germany, 2009.
36. Arakaki, L.S.; Burns, D.H.; Kushmerick, M.J. Accurate myoglobin oxygen saturation by optical spectroscopy measured in blood-perfused rat muscle. *Appl. Spectrosc.* **2007**, *61*, 978–985. [[CrossRef](#)]
37. Taylor, J.R. An Introduction to Error Analysis: The Study of Uncertainties in Physical Measurements. *University Science Books*; Oxford University Press: Mill Valley, CA, USA, 1982

- 
38. Taroni, P.; Comelli, D.; Farina, A.; Pifferi, A.; Kienle, A. Time-resolved diffuse optical spectroscopy of small tissue samples. *Opt. Express* **2007**, *15*, 3301–3311. [[CrossRef](#)] [[PubMed](#)]
  39. Rejmstad, P.; Zsigmond, P.; Wårdell, K. Oxygen saturation estimation in brain tissue using diffuse reflectance spectroscopy along stereotactic trajectories. *Opt. Express* **2017**, *25*, 8192–8201. [[CrossRef](#)] [[PubMed](#)]